Research Square

Preprints are preliminary reports that have not undergone peer review.
They should not be considered conclusive, used to inform clinical practice,
or referenced by the media as validated information.

Forward mass flow and melt pool tailoring in keyhole laser welding driven by high frequency two-point longitudinal beam oscillation

Aurelien Wohrer
Empa Thun Branch: EMPA Thun Standort
Evangelos Skoulas
evangelos.skoulas@empa.ch
Empa Materials Science and Technology: Empa https://orcid.org/0000-0001-8926-048X
Pinku Yadav
Empa Thun Branch: EMPA Thun Standort
Chang Rajani
Empa Thun Branch: EMPA Thun Standort
Alexander Rack
ESRF
Elia Iseli
Empa Thun Branch: EMPA Thun Standort

Research Article

Keywords: Laser welding, Beam oscillation, Keyhole dynamics, Melt pool, Mass transport, In situ X ray imaging

Posted Date: November 12th, 2026

DOI: https://doi.org/10.21203/rs.3.rs-11113082/v1

License: This work is licensed under a Creative Commons Attribution 4.0 International License.
Read Full License

Forward mass flow and melt pool tailoring in keyhole laser welding driven by high frequency two-point longitudinal beam oscillation

Aurélien Wohrer[1], Evangelos Skoulas[1*], Pinku Yadav[1], Chang Rajani[1], Alexander Rack[2], Elia Iseli[1]

[1] EMPA, Laboratory for Advanced Materials Processing, Feuerwerkerstrasse 39, 3602 Thun,Switzerland

[2] ESRF – The European Synchrotron, CS 40220, Grenoble, F-38043, France

Corresponding author: evangelos.skoulas@empa.ch

ABSTRACT

Melt pool geometry in laser welding is usually tuned through laser power, scanning speed and beam profile. Here we show that beam wobble can instead tailor its width, depth and shape at constant power and speed, and also impose a directed mass flow inside the pool. Three two point patterns along the scan direction, balanced, front heavy and back heavy, are studied on 316L steel at 1 to 4 kHz and 0 to 1000 µm amplitude, using metallography and in situ synchrotron X ray imaging at 50,400 frames per second. Amplitude alone drives three regimes: a deep, narrow melt pool with a stationary keyhole at low amplitude, an unstable regime at 100 to 300 µm where porosity peaks near 200 µm, and a restabilized onion shaped melt pool above about 400 µm where the keyhole forms only at the extremities. Rear preheating enlarges the rear keyhole, and the resulting pressure asymmetry drives a drag dominated flow that sweeps pores forward for reabsorption. Tracking pores as flow tracers gives forward velocities of up to 240 µm/ms, and the fraction carried forward rises from one half without oscillation to 0.88 at 800 µm. The balanced pattern gives the fastest flow, reaches the onion shape at the lowest amplitude and keeps the deepest penetration up to about 450 µm. The pool contents are swept from rear to front several times before solidification. Dwell distribution, amplitude and frequency thus control both melt pool geometry and internal mass transport at fixed power and speed.

Keywords: Laser welding; Beam oscillation; Keyhole dynamics; Melt pool; Mass transport; In situ X ray imaging

1. INTRODUCTION

Within a decade of the first demonstration of laser operation in 1960, laser welding was already investigated as a promising joining technique for a wide range of materials with confined heat affected zone and distortion[1–3]. Beam wobbling has emerged as a promising strategy for improving process stability, melt pool control, and joint quality in laser-based manufacturing processes. Recent studies have demonstrated its effectiveness in laser beam welding, and hybrid additive manufacturing, where oscillation can reduce porosity, enhance mixing, and improve mechanical performance[4–6]. Most investigations have concentrated on a limited set of canonical trajectories such as linear longitudinal, and circular oscillations often reported as particularly effective for improving weld quality and homogenization[9,10]. More complex or non-standard trajectories remain relatively underexplored, with only a few studies reporting alternative designs such as flower shaped or engineered oscillation paths that can further improve weld formation and energy distribution[11,12].

Despite becoming a well established industrial process [1–3,13] fine control of the melt pool geometry and keyhole dynamics in laser beam welding remains challenging, as both are highly sensitive to process parameters[9,11,14,15]. However, most studies have focused on only a limited set of oscillation patterns, primarily transverse, longitudinal, and circular, with circular oscillation most frequently identified as the most effective [7,10,16]. Alternative beam trajectories remain largely unexplored, with only a few exceptions, such as the flower shaped pattern proposed which showed improved performance in lap joint welding [17]. In addition, low to intermediate frequency oscillation (<1kHz) has been widely reported in the literature [6,18], systematic investigations in the multi kilohertz regime remain relatively limited [19,20], indicating the need for further research. A further limitation is that oscillation is almost always judged by the shape it leaves behind, through weld width, penetration depth and pore count measured after solidification. What happens to the material inside the pool while it is still liquid is rarely measured, even though it governs mixing in dissimilar joints and whether a pore reaches the keyhole before the solidification front reaches it. In situ synchrotron X ray imaging removes this limitation, resolving the keyhole and individual pores at microsecond scale [8,21,22], and once pores are shown to follow the surrounding liquid rather than moving under their own buoyancy they become tracers of the melt flow itself. The key challenge remains the active control of the melt pool geometry and keyhole dynamics, which govern weld quality and are highly sensitive to common process parameter (power, scanning speed, beam profile).

The objective of this study is to investigate how high frequency two point beam wobbling can be used to tailor melt pool geometry, and the mass transport within it, without modifying the primary welding parameters, such as laser power or welding speed. A two point oscillation collinear with the scan direction is employed, and three custom wobbling patterns are examined: a balanced pattern, a front heavy pattern, and a back heavy pattern, each defined by different dwell time distributions at the two oscillation extremities. The two dwell points are thermally distinct by construction, because the rear point re enters material that the previous dwell has already heated while the front point meets fresh material. Welding experiments are conducted over a range of oscillation amplitudes (A = 0–1000 μm) and frequencies (f = 1–4 kHz), and the resulting melt pool geometries are characterized through cross sectional metallography. In situ synchrotron X ray imaging was used to directly observe keyhole dynamics, melt flow behavior, and porosity formation in real time, providing mechanistic insight into the process transitions occurring across the investigated parameter space. Tracking pores across the full recordings yields the forward velocity, the fraction of material carried forward and the resulting mass flux, showing that the wobbling pattern, amplitude and frequency all govern the rate at which melt is transported from the rear of the pool to the front. These findings are discussed in the context of

potential applications, including micro welding, where precise control of melt pool dimensions at specific depths is critical, and multi material joining, where the enhanced internal melt flow observed at high amplitudes and frequencies can be leveraged to promote mixing and improve interfacial bonding.

2. METHODOLOGY

The experimental setup described in Figure 1a consists of a Rofin laser source (λ = 1070 nm) equipped with a Coherent PH-10 wobble-head, whose controller is not depicted in the Figure 1a. Inside the head, the beam passes through a collimation unit, is steered by a galvanometer scanner consisting of two mirrors and then focused onto the plate by a convex lens with a focal length of 200 mm, forming a spot size of 36µm ($1/e^2$) at the surface. A nozzle positioned at 45° with respect to the plate provides a continuous flow of argon at a flowrate of 15 l/min, creating a protective atmosphere that minimizes oxidation during the welding process. The plate is attached to a moving axis that translates it horizontally to the left while the wobble head remains stationary, thereby inducing a scanning direction to the right. In addition to this scanning movement, the wobble head oscillates the beam back and forth to create a two-point pattern that is longitudinal, lying on the same axis as the scanning direction.

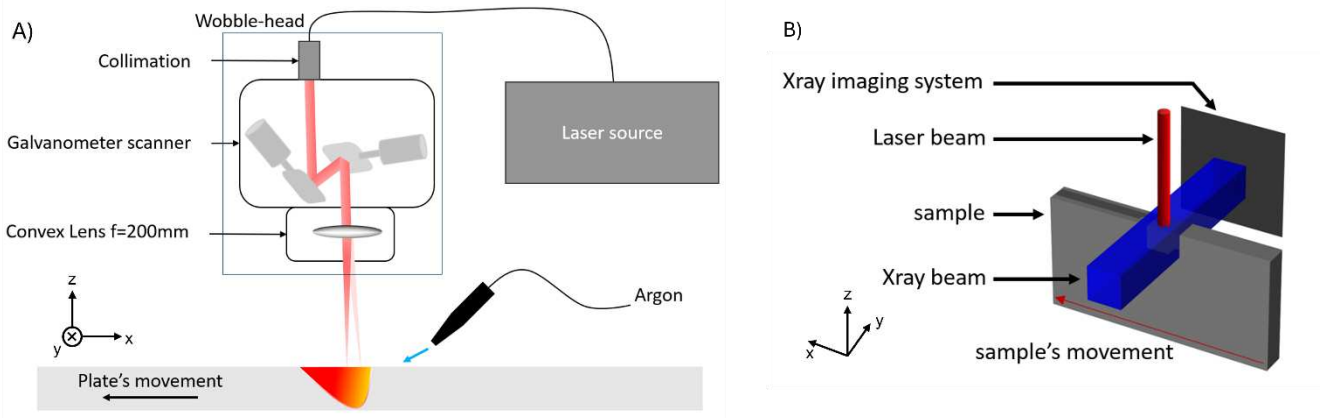


Figure 1:(a) schematic of the wobbling setup and (b) Schematic of the X-ray imaging setup.

The imaging setup for the synchrotron video is illustrated in Fig. 1(B). The hard X-ray beam is oriented normal to both the scanning direction and the laser beam, enabling in-situ visualization of the welding process from the side, complementary to the metallography cross-sections. As shown in the schematic Fig. 1(B), the laser beam is incident vertically onto the sample from above at normal incidence, while the sample is oriented edge-on to a horizontal X-ray beam that passes through it; an X-ray imaging system positioned on the opposite side records the transmitted beam, and the sample translates relative to the laser (indicated by the "sample's movement" arrow), allowing the interaction zone to be imaged during processing. The rest of the setup is identical to the wobbling configuration described in Fig.1(A). Experiments were carried out at the full-field imaging beamline ID19 of the European Synchrotron ESRF (Grenoble, France). The beamlines single-harmonic undulator (type: u17.6, gap 14.4, nominal peak photon energy 18 keV) was used without any additional X-ray optical elements besides the mandatory diamond and Beryllium windows: this white-beam configuration allows intense photon flux density in combination with outstanding sensitivity by means of X-ray phase contrast imaging. The required high-speed imaging detector was positioned 3.5 m downstream of the sample. It consist of a 100 µm-thick LuAG:Ce single-crystal scintillator (Crytur, Czech Republic): its luminescent image is projected by a long-working microscope lens (10× magnification / 0.28 numerical aperture, Mitutoyo, Japan) via a mirror onto the CMOS-sensor of a high-speed camera (type: SAZ, Photron Corp., Japan). Images are acquired with a nominal pixel size of 2.2 µm[21].

The material used is 316L steel, supplied as a 200 × 120 × 2.15 mm3 plate for the metallography investigations and as 40 × 1.5 × 20 mm3 samples for the synchrotron measurements. The influence of individual process parameters, namely the pattern type, A, and f is investigated by varying each parameter independently. The power was kept constant at 100 W for all experiments, while the sample movement speed was 3 mm/s for the bulk samples and 6 mm/s for the synchrotron measurements. This difference in speed means that each set of results must be treated independently; nevertheless, the results are quite similar in terms of weld depth, as the higher speed used for the synchrotron samples compensates for the lower heat dissipation arising from the sample geometry.

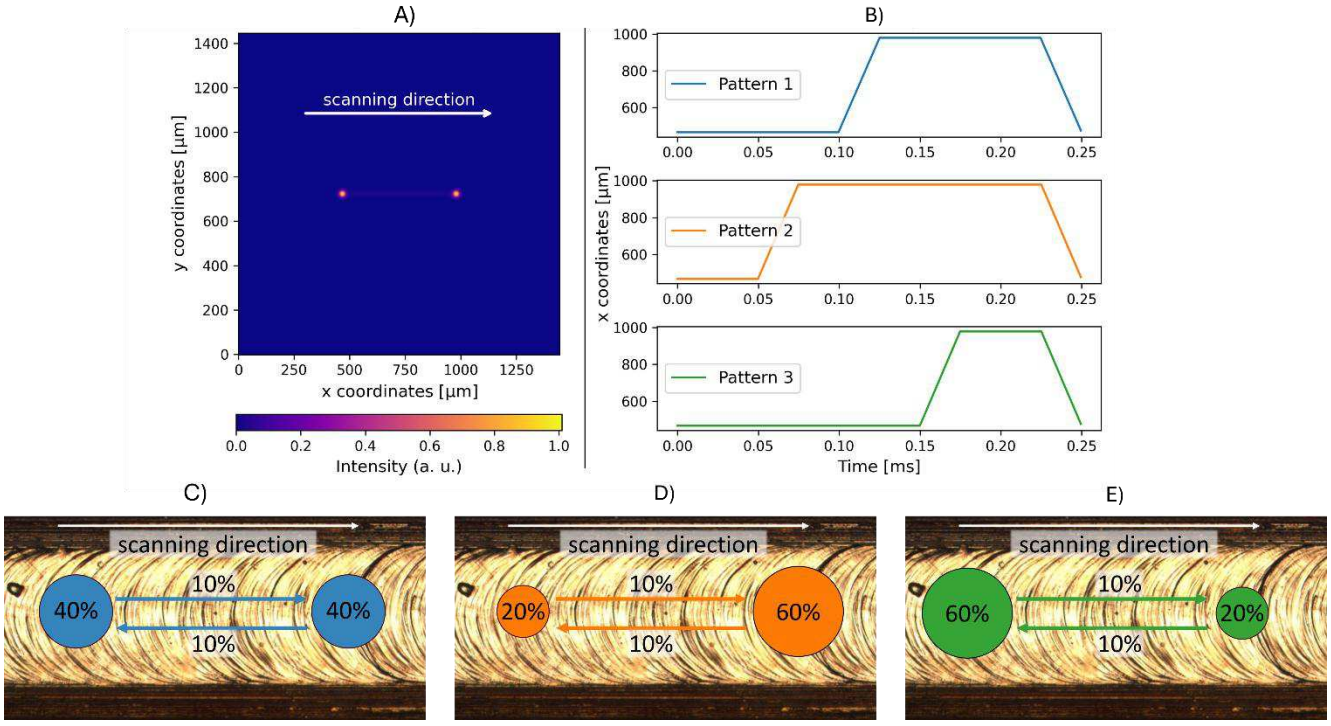


Figure 2: (a) left: example of the intensity distribution over one cycle of the pattern 1.(b) x coordinate over time of the patterns 1, 2 and 3 with F = 4kHz (balanced, front-heavy and back-heavy respectively) Both the pattern and the scanning direction are on the x-axis. right: x coordinate over time of the patterns 1, 2 and 3 with F = 4 kHz (balanced, front-heavy and back-heavy respectively (c), (d)and (e) Schematic explanation of patterns 1, 2 and 3 respectively, the percentage/size of the circle represents the beam dwell time with neglecting the sample motion.

The wobbling strategy examined in this study is a custom-designed longitudinal two-point pattern, with its different versions shown in Fig. 2 for a f = 4 kHz. In Fig. 2A the blue beam intensity maps the accumulated energy over one complete wobble cycle for pattern 1, plotted against x and y (both in µm) and normalized to the maximum value. The scanning direction and the wobble oscillation are collinear, both lying along the x-axis, and the deposited intensity is confined to a narrow horizontal band centered at y ≈ 720 µm. Two intense spots appear within this band, near x ≈ 480 µm and x ≈ 990 µm, separated by roughly 500 µm, which corresponds to the peak-to-peak wobble span. These spots mark where the beam dwells longest and accumulates the most fluence, while the faint line connecting them is the lower-fluence region crossed rapidly during transit. For pattern 1 the two spots are of comparable brightness, reflecting its balanced dwell distribution.
Fig.2(B) shows the beam x position as a function of time over one cycle for all three patterns at f= 4 kHz, giving a cycle period of 0.25 ms that matches the time span of each trace. Each trace is trapezoidal: the beam holds at the rear (≈ 500 µm), ramps quickly to the front (≈ 980 µm), holds there, and ramps back. The transits are short in every case, while the two dwell segments differ in duration and define the pattern. In pattern 1 (balanced) the dwell time is split evenly between the two ends, in

pattern 2 (front-heavy) most of the cycle is spent at the front, and in pattern 3 (back-heavy) most of it is spent at the rear.
The aim of this pattern is to create two alternating heating locations within the melt pool, one at the front and one at the rear, so that the underlying thermophysical effects could be investigated. Other wobbling patterns were also tested, but all of them produced large amounts of residual porosity across their full parameter range. The schematics in Fig. 2 (C-E) make the dwell distribution explicit, each overlaid on a weld track with the scanning direction toward the right. The two-colored circles mark the beam end positions, the left one the rear and the right one the front with the percentage in each giving the fraction of the cycle spent dwelling there and the arrows labelled with the transit fractions. In all three versions the beam starts on the left point, where it remains for 40 %, 20 %, or 60 % of the period for patterns 1, 2, and 3. It then moves to the right point over 10 % of the period, where it stays for 40 %, 60 %, or 20 %, and finally return to the left during the last 10 %. The sample's motion is neglected in computing the beam dwell time percentages. Since the two transits each take 10 %, the dwell and transit fractions sum to 100 %, and the balanced, front-heavy, and back-heavy labels simply describe whether the dwell time is even, biased toward the front or biased toward the rear relative to the scanning direction. The A stands always as physical, the distance between the two points.

3. Results and Discussion

3.1. Metallographic cross-section results

Metallographic analyses were carried out on cross-sections of welds produced with each pattern at a f = 4 kHz and varying oscillation amplitudes. The results show that the melt pool shape can be controlled by adjusting the oscillation amplitude. Qualitative information about the melt pool shapes for pattern 1 is presented in Figure 3, which shows four transverse cross-sections produced at f = 4 kHz with the amplitude increased across the panels. In each image the melt pool is highlighted in pink against the orange-brown etched base material, a thin blue layer marks the top surface. At Fig.3A, A = 0 μm (no wobbling), the fusion zone is narrow and deep, with a slender, dagger-shaped profile that tapers to a point at its base, characteristic of a stationary, deeply penetrating beam. At Fig.3D, A = 48 μm the cross-section remains narrow and deep, broadly similar to the no-wobble case, with only the upper region appearing marginally wider. For amplitudes below 50 μm, then, beam wobbling does not significantly modify the melt pool geometry. The profile changes markedly at Fig.3C at A = 200 μm, where the fusion zone becomes distinctly wider near the surface, adopting a broader, more triangular shape that still tapers toward a point, with reduced penetration depth and two small pores visible within the fused region. By A = 504 μm the fusion zone is broad and rounded near the top, forming a wide, onion-shaped cap with a thin spike extending downward toward the root. Overall, Figure 3 illustrates a progressive shift from a deep, narrow fusion zone at low amplitude to a broad, shallow cap with a narrow downward protrusion at high amplitude, the width increasing and the penetration depth decreasing as the amplitude grows.

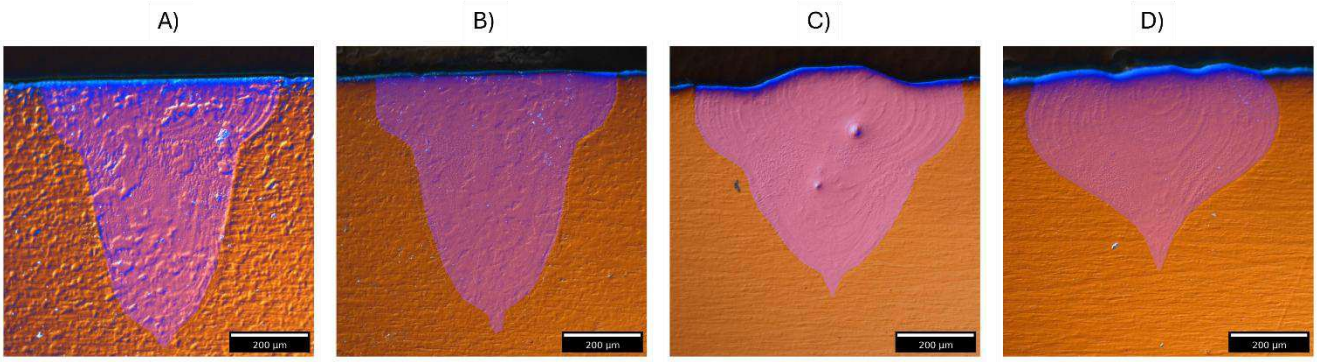


Figure 3: Cross-sections of welds with pattern 1 at 4 kHz with different amplitudes A (meltpools are highlighted in pink). a) A = 0µm (no wobbling) b) A = 48µm c) A = 200µm d) A = 504µm

Following this trend, an amplitude of 200 µm gives a shallower, slightly wider melt pool that contains residual porosity, and the melt pool becomes gradually shallower at higher amplitudes. Once the oscillation amplitude exceeds 400 µm, an onion-shaped melt pool forms, as shown in Figure 3d. For patterns 2 and 3, this onion-shaped morphology appears only at amplitudes of 600 µm and above.
To obtain quantitative information, the melt pool depth and width were measured for three repetitions of each parameter combination, and the averaged values were used to generate the trends in Figure 4. Below an amplitude of about 450 µm, pattern 1 maintains a deeper melt pool than patterns 2 and 3. The surface width for pattern 1 drops at A = 400 µm as it shifts to an onion-shaped melt pool, while for pattern 3 the width drops at A = 600 µm and for pattern 2 at A = 800 µm for the same reason. For patterns 2 and 3, amplitudes above 800 µm lead to a marked reduction in melt pool dimensions, since the material is able to partially solidify between the two heating spots.

Quantitative values of the melt pool cross-section as a function of the wobble A are summarized in Figure 4, combining a metallographic optical microscopy image that defines the measured dimensions with two scatter plots reporting those dimensions for the three patterns and the non-wobbled reference.

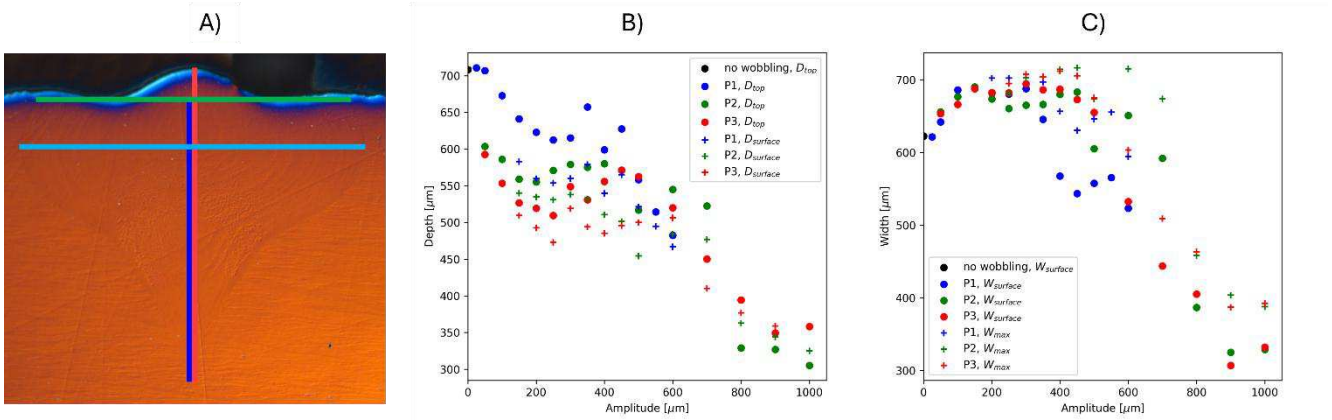


Figure 4: Geometry of the meltpools as a function of the amplitude A: (A) the measurement scheme is composed of the width at the surface of the sample (Wsurface) denoted with green line, the maximum width (Wmax) with cyan line, the depth from the top of the weld (Dtop) with blue line and the depth from the surface of the sample (Dsurface) with red line. (B) Dtop of the weld (•) and Dsurface of the sample (+) with regard to the A of the pattern. The Dtop of the weld for Pattern 1 (•) is superior to that of the other patterns until A = 450µm. (C) Wsurface of the sample (•) and Wmax (+) with regard to the amplitude of the pattern. The width at the surface for pattern 1 (•) drops at A = 400µm.

The measurement scheme in Figure 4a is illustrated on a transverse cross-section with the weld region at the top of the base material in orange and four colored lines marking the extracted quantities. The green horizontal line denotes the width at the surface level, $W_{(surface)}$, the cyan horizontal line the maximum width, $W_{(max)}$, located below the surface at the widest part of the fusion zone, the red

vertical line the depth measured from the top of the weld cap, $D_{(top)}$, and the blue vertical line the depth measured from the sample surface, $D_{(surface)}$. The two depth definitions differ because the weld cap may protrude above the original sample plane, so $D_{(top)}$ is referenced to the highest point of the weld and $D_{(surface)}$ to the sample surface.
In Figure 4b the depth is plotted against the amplitude, with depth on the vertical axis (about 300 to 700 μm) and amplitude on the horizontal axis (0 to 1000 μm). Filled circles denote the depth from the top of the weld and plus signs the depth from the surface, while color identifies the condition: black for the non-wobbled reference, blue for pattern 1, green for pattern 2, and red for pattern 3. Depth decreases overall with increasing amplitude, falling from around 700 μm at low amplitude to roughly 300 to 350 μm near A = 1000 μm, and for each pattern the plus signs sit systematically below the corresponding circles, reflecting the offset between the two reference planes. The depth from the top of the weld for pattern 1 remains the largest up to about A = 450 μm, so pattern 1 achieves the deepest penetration over this range, beyond which it no longer exceeds the other patterns.
In Fig.4(C) the width is plotted against the amplitude using spans of roughly 300 to 700 μm and 0 to 1000 μm respectively. In contrast to the depth, the width first increases with amplitude, reaching its highest values of around 700 μm in the intermediate range of about A ≈ 100 to 400 μm, then decreases at larger amplitudes toward 300 to 450 μm near A = 1000 μm. The surface width for pattern 1 shows a pronounced drop at A = 400 μm.
Taken together, Fig.4(B) and Fig.4(C) reveal opposite tendencies of the two dimensions with amplitude: the penetration depth falls progressively as the amplitude grows, whereas the width passes through a maximum at intermediate amplitude before decreasing. Pattern 1 stands out both for the deepest penetration up to A = 450 μm and for the marked reduction in its surface width at A = 400 μm, identifying A ≈ 400 μm as the point where its behavior changes relative to the other patterns.

3.2. SYNCHROTRON RESULTS

Figure 5 presents successive snapshots of the synchrotron radiography videos, which were recorded at a frame rate of 50,400 fps and post-processed with a home-made Python script relying mainly on the cv2 module of the OpenCV library. The frames are arranged as a matrix in which each row corresponds to a different wobble amplitude and each column to a successive instant within the cycle. The amplitudes increase down the rows while the columns span one cycle in equal steps from 0.00 to 0.24 ms, consistent with the 0.25 ms period of the 4 kHz oscillation. Each frame covers a field of view of 1.27 mm × 0.74 mm, with the sample surface near the top, and the transmitted X-ray contrast reveals the sub-surface features of the process: the keyhole appears as a dark, elongated intrusion extending downward from the surface, while pores and gas bubbles within the melt appear as small, rounded features beneath it.

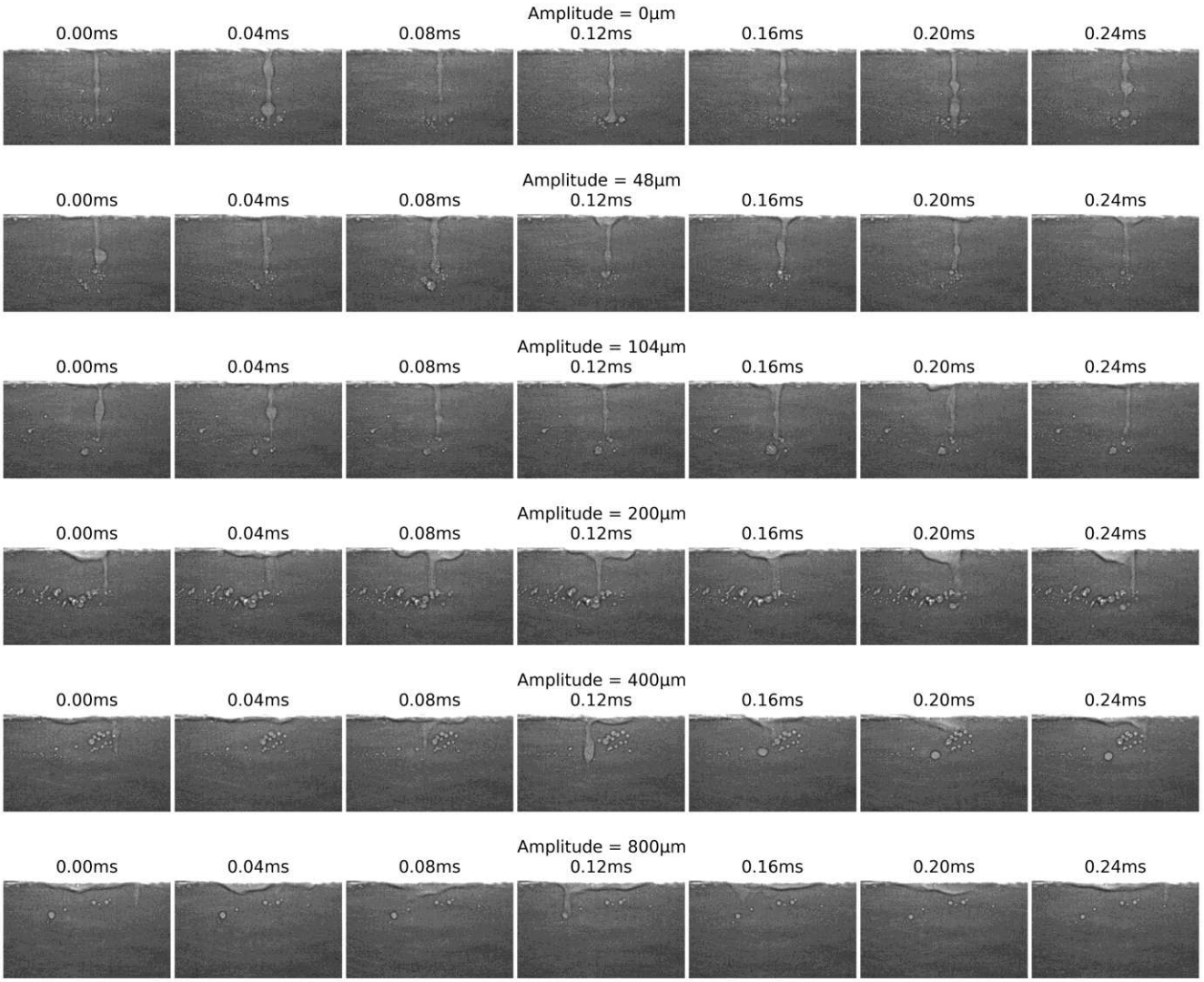


Figure 5: Snapshots of the welding process at various amplitudes over one pattern (scale: the snapshots are 1.27mm x 0.74mm). At A = 200µm, we can see the keyhole moving around the meltpool. At A = 400µm and 800uµm, the keyhole is only formed at the extremities of the meltpool.

There is minimal visible difference between no wobbling and wobbling at amplitudes below 100 µm. At the lowest amplitudes the keyhole is narrow, deep, and approximately vertical, staying close to a fixed lateral position as the cycle progresses; this holds for A = 0 µm and is broadly retained at A = 48 µm and A = 104 µm, where the keyhole remains slender and deep with only limited lateral movement and a modest population of bubbles below. At A = 200 µm the behavior changes, as the keyhole becomes shallower and moves laterally across the melt pool over the cycle, following the movement of the laser spot, while the number of bubbles along the melt pool increases. At A = 400 µm and 800 µm the keyhole is no longer maintained continuously: the melt pool is broad and shallow, and a keyhole forms only at the extremities of the oscillation, where the beam dwells longest, and is essentially absent through the central part of the traverse. At these two amplitudes the keyhole at the back of the melt pool (at 0.12 ms) is also much larger than the one at the front (at 0.00 ms and 0.24 ms), because the keyhole at the back forms in much hotter material, whereas fresh material arrives at the front. Across the six amplitudes, the sequence therefore documents a progressive transition with increasing amplitude: from a stationary, deep keyhole near A = 0 µm, through a shallower keyhole that migrates around the melt pool at A = 200 µm, to a regime at A = 400 µm and 800 µm in which the keyhole is confined to the extremities of the pattern and the melt pool becomes wider and shallower.

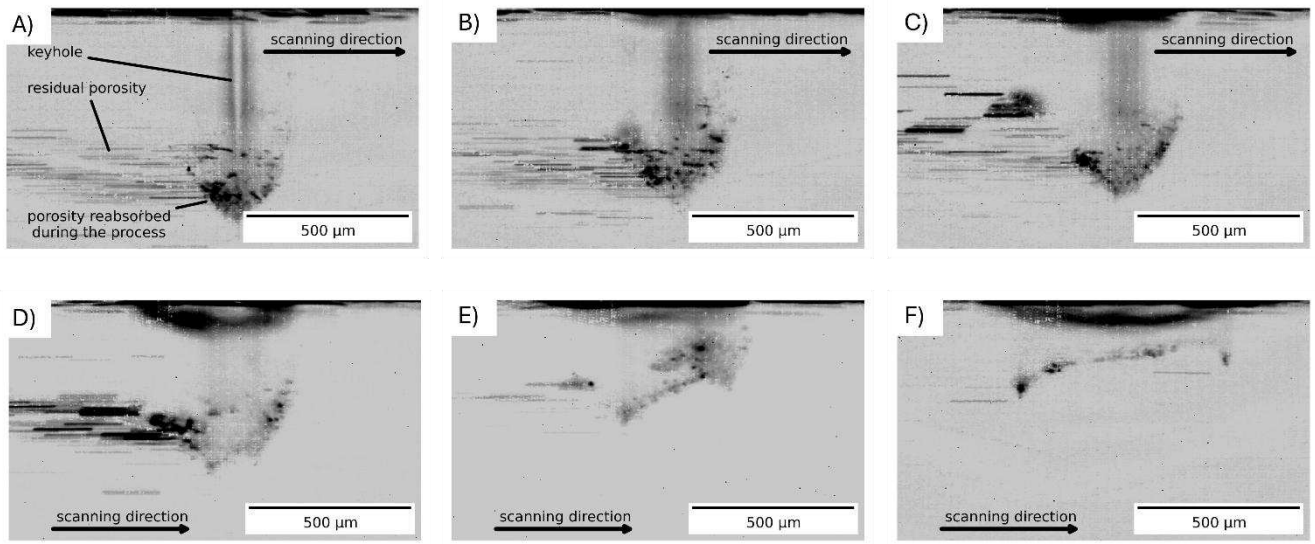


Figure 6: Variance over time of the synchrotron videos (side-view of the process) for different amplitudes A with pattern 1 at F = 4kHz (A) no wobbling, (B) A = 48µm, (C) A = 104µm, (D) A = 200µm, (E) A = 400µm and (F) A = 800µm.

The snapshots in Figure 5 are limited for drawing firm conclusions, since they show only a fraction of each video. It is possible to capture a whole video at once using the temporal variance of the pixel intensities: each video is treated as a 3D array, and taking the variance over the third dimension (time) reduces it to a 2D image.

Figure 6 shows the temporal variance of the synchrotron videos (side view) for the six amplitudes A = 0, 48, 104, 200, 400, and 800 µm, all with pattern 1 at f = 4 kHz. Since each image is the variance of the signal over the whole video rather than a single instant, moving or fluctuating regions appear dark while static ones appear light, making these maps a convenient way to visualize the cumulative envelope of the keyhole motion and the porosity trajectories over a full cycle. Each panel has a 500 µm scale bar and an arrow for the scanning direction. In the Figure 6a, A = 0 µm with no wobbling, the keyhole fluctuations appear on each side of the keyhole, the black dots at the bottom of the melt pool are porosity reabsorbed by the keyhole, and the dark horizontal lines are residual porosity. As the amplitude increases, the dark keyhole region broadens because it now sweeps laterally rather than staying fixed: in Figure 6b A = 48 µm the dark vertical region marks this lateral movement, with comparable behavior in Figure 6c A = 104 µm. In Figure 6d A = 200 µm the residual porosity is very high compared with the other amplitudes, and the melt pool floor shows two distinct extremities separated by a shallower central region, characteristic of the two-point pattern. In Figure 6e A = 400 µm the dark oblique line at the bottom of the melt pool stems from porosity moving from the back toward the front, and Fig.6(F) completes the series at A = 800 µm.
These regimes reflect a transition in keyhole behavior: at low amplitudes the keyhole follows the imposed scanning pattern, whereas at high amplitudes it only forms at the extremities of the oscillation. Figure 6e-f, the keyhole at the back of the melt pool is larger than the one at the front, indicating higher temperatures at the back, and the porosity is seen to migrate from the back toward the front. Hojjatzadeh et al. [8] showed that pores near the laser are drawn back toward the keyhole by a thermocapillary force, while away from it the dominant agent is the drag exerted by the surrounding melt, buoyancy being negligible in both regions. The migration observed here occurs along the pool floor, away from either keyhole, so it should result from a flow of melt from the back to the front of the melt pool.
Across the six panels, the variance maps trace the same amplitude-dependent transition seen in the

instantaneous snapshots, now as the time-integrated footprint of the dynamics: a narrow keyhole with side fluctuations and reabsorbed porosity at A = 0 µm, a progressively broader band marking the lateral sweep at intermediate amplitudes, a two-extremity melt pool floor with pronounced residual porosity at A = 200 µm, and oblique porosity trajectories within a wide, shallow melt pool at the largest amplitudes.

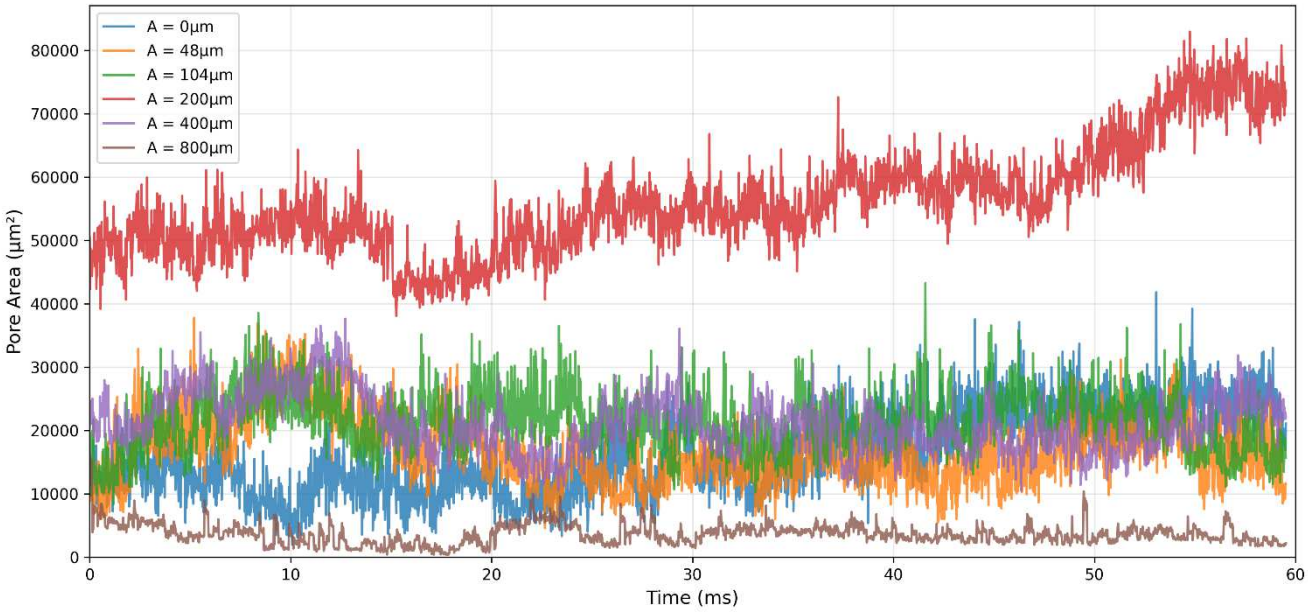


Figure 7: Porosity vs amplitude for pattern 1.

Figure 7 plots the porosity area measured in the x-ray video recordings for the results presented at Fig.5 and Fig.6 as a function of time for the six amplitudes. The videos were treated through a machine learning model: the raw images were segmented into masks where each pixel was assigned either 0 (background), 1 (keyhole) or 2 (porosity), with the help of the model presented at [22].We fine-tuned the model with some of our images to increase its accuracy on our dataset. The model does not differentiate between porosity that is reabsorbed and residual porosity. In Fig.7 the number of pixels that were assigned the value 2 in each frame (with a conversion factor of 4.494 um^2 per pixel) is plotted. Here, pore area (µm²) on the vertical axis spanning roughly 0 to 80,000 µm² and time (ms) on the horizontal axis covering about 0 to 60 ms. Each A is a separate trace, color-coded as A = 0 µm in blue, 48 µm in orange, 104 µm in green, 200 µm in red, 400 µm in purple, and 800 µm in brown. All traces fluctuate strongly from point to point, reflecting the frame-by-frame nature of the measurement, so the meaningful comparison is between the overall levels and trends rather than the instantaneous values. The curve for A = 200 µm stands clearly apart, occupying the upper part of the plot throughout: it begins around 45,000 to 55,000 µm², passes through a shallow minimum near t ≈ 15 to 20 ms, then rises progressively to about 70,000 to 80,000 µm² by t ≈ 55 to 60 ms, showing both the largest porosity area and a marked upward trend, consistent with the high residual porosity noted for this amplitude in the earlier figures. The amplitudes A = 0, 48, 104, and 400 µm form a densely overlapping intermediate band, fluctuating between about 10,000 and 35,000 µm² across the whole duration and crossing repeatedly, with none showing the systematic growth seen at A = 200 µm. The curve for A = 800 µm lies consistently at the bottom, at roughly 3,000 to 10,000 µm² throughout, giving the smallest porosity area of all. Overall, the porosity area is by far the greatest and grows over time at A = 200 µm, is intermediate and comparatively stable for the cluster of low and moderate amplitudes meaning that most of the porosity is reabsorbed by the keyhole during the welding process and is lowest at the

largest amplitude, A = 800 µm. It is important to note that we can observe that the amount of porosity is three times higher in the case of 200µm and almost negligible in the case of 800µm. At all the other amplitudes, the porosity is equivalent to the amount of porosity of a weld without wobbling. The upward trend at A = 200 µm should be read with the field of view in mind. At 6 mm/s a pore requires about 100 ms to leave the laser fixed field of view, longer than the 59.5 ms recording, so residual pores accumulate within the frame and part of the rise reflects this accumulation rather than continued generation.

Figure 8 compares the porosity movement in the synchrotron videos for the three patterns at f = 4 kHz and a fixed amplitude of A = 800 µm. The first part is arranged in three rows, one per pattern, with six consecutive snapshots along each row taken at 0.00, 1.98, 3.97, 5.95, 7.94, and 9.92 ms, followed by a variance-over-time image in the rightmost column, each frame spanning a field of view of 1.27 mm × 0.74 mm. Colored markers are overlaid on the snapshots to label individual pores so that their trajectories can be followed from frame to frame. The variance images at the right of each row summarize the time-integrated dynamics: all three patterns display an oblique dark line at the bottom of the melt pool, highlighting the direction of material flow within the pool, while the upper region appears more unstable for pattern 3 than for the other two. Combined with the tracked snapshots, these maps confirm that the labelled pores migrate along the melt pool floor in a consistent oblique direction over the recording.
The accompanying plot reports the forward velocity of every pore tracked automatically across the full recording, with forward velocity (µm/ms) on the vertical axis and the three patterns along the horizontal axis, color coded blue for pattern 1, orange for pattern 2 and green for pattern 3. Velocities are referred to the surrounding material rather than to the camera, which is fixed to the laser, and therefore include the 6 µm/ms of sample translation. Pattern 1 gives the highest mean forward velocity at 49.8 ± 45.9 µm/ms over 23 forward moving pores, pattern 2 follows at 38.6 ± 37.6 µm/ms over 38 pores, and pattern 3 is the slowest at 18.1 ± 12.0 µm/ms over 18 pores. The fraction of pores carried forward is 0.88, 0.90 and 0.78 respectively. The ordering indicates that the balanced pattern drives the fastest material flow in the melt pool, and that biasing the dwell toward the rear slows it most.
The movement of the pores from back to front along the scanning direction, together with their resorption when they reach the keyhole at the front, was consistently observed for all patterns tested. Taken together, the snapshots and the speed measurements link the qualitative observation of oblique porosity trajectories in the variance images to a quantitative measure of flow velocity, showing that at A = 800 µm the three patterns drive measurably different rates of pore transport, with pattern 1 the fastest and pattern 2 the slowest. The faster material flow generated by pattern 1 could explain why it transitions to the onion-shaped melt pool at lower amplitudes than patterns 2 and 3. This enhanced flow may reflect an imbalance between driving forces (e.g., temperature and pressure gradients) and resisting effects (e.g., viscosity and surface tension), potentially leading to stronger convective motion in pattern 1.

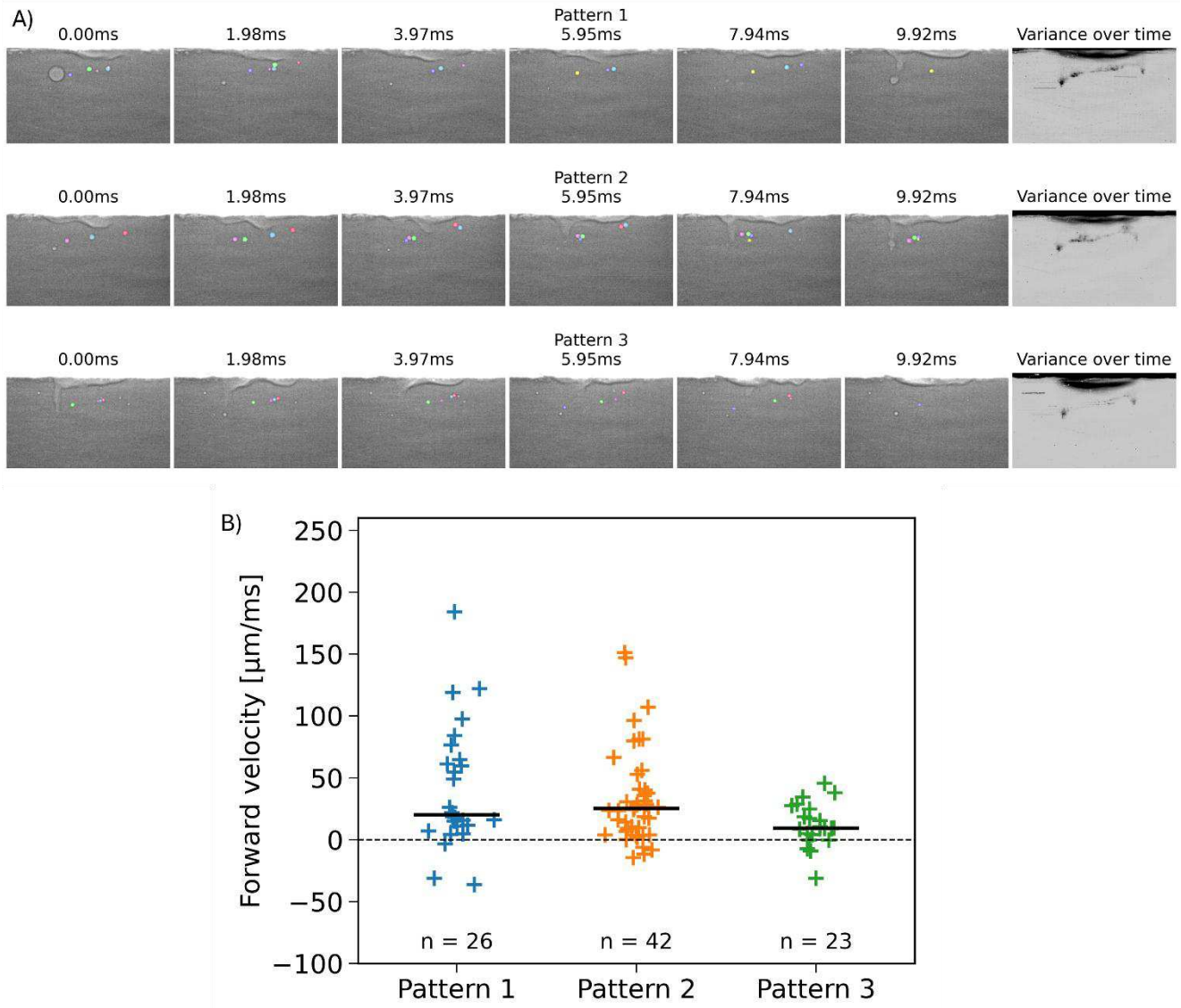


Figure 8: Comparison of the porosity movement in the x-ray videos for the 3 different patterns with f = 4kHz and A = 800µm: (A) The rightmost image is the variance over time of the video. All three patterns present an oblique dark line at the bottom of the meltpool, highlighting the material flow in the meltpool. The top of the meltpool is more unstable in pattern 3. The snapshots allow to visually follow the trajectory of some pores (scale: the snapshots are 1.27mm x 0.74mm). (B) Forward velocity of every pore tracked automatically over the full 59.5 ms recording, for each of the three patterns, referred to the surrounding material. Horizontal bars mark the median and n is given per pattern.

Figure 9 presents the temporal variance of the synchrotron videos, again in side view, this time for a fixed pattern (pattern 1) and a fixed amplitude of A = 800 µm while the wobble f is varied across the four images from Figure 9a: f = 1 kHz , Figure 9b: f = 2kHz, Figure 9c:f=3 kHz and Figure 9d:f = 4 kHz. As in the earlier variance figures, fluctuating regions register as dark and static regions as light, so the images map the time-integrated envelope of the keyhole motion and the porosity trajectories over the recording. Each image carries a 500 µm scale bar and a scanning-direction arrow pointing to the right.

At the lowest f = 1 kHz, the variance map shows two well-separated dark concentrations, one toward the left and one toward the right of the field of view, corresponding to the two dwell extremities of the pattern, with a comparatively clear region between them and several short dark horizontal lines marking residual porosity implying that the central region is solid or at least very viscous as the

porosities form straight lines, i.e. they do not move. The two keyhole footprints are therefore distinct and largely independent, with little activity in the intervening melt pool. As the frequency increases, the region between the two extremities becomes progressively more active. At f = 2 kHz the two dark extremities persist but an oblique dark feature begins to connect them, curving upward toward the top of the melt pool and indicating material transport between the dwell points. This trend continues at f = 3 kHz, where the oblique band linking the back extremity toward the front is more developed, and is most pronounced at 4 kHz, where a continuous arc of dark features extends across the upper part of the melt pool between the two extremities, reflecting more sustained porosity and material movement along the pool. Across the four frequencies, then, the two characteristic dwell extremities of pattern 1 are preserved at constant amplitude, while the degree of connection between them grows with frequency, the transport of porosity and the associated material flow becoming increasingly continuous as f is raised from 1 kHz to 4 kHz.
Tracking the keyhole position frame by frame gives a dwell point separation of 628 µm at 4 kHz, 79 % of the imposed amplitude of 800 µm, against 808, 833 and 810 µm at 1, 2 and 3 kHz, which are the full amplitude within the measurement scatter. The measured oscillation frequency matches the commanded value to within 0.1 % in every case, so the shortfall is not a timing error. This is explained by the fact that the keyholes are not fully formed at 4 kHz: they start forming ahead of the stationary points in the pattern and do not have time to migrate to the stationary point position before the laser spot crosses the melt pool again.

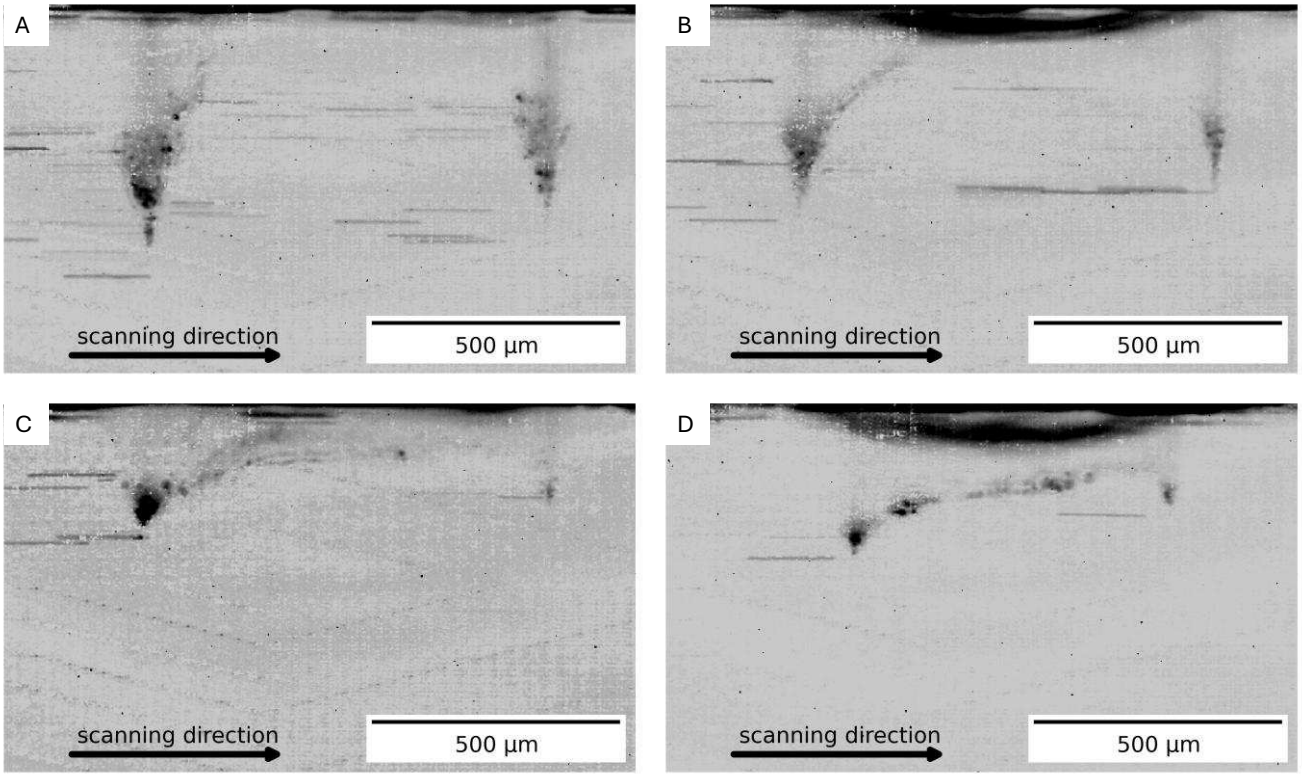


Figure 9: Variance over time of the synchrotron videos (side-view of the process) for different f values with pattern 1 at A = 800µm. The oscillationg f range from (A) f=1kHz, (B) f=2kHz, (C) f=3kHz and (D) f=4kHz.

3.3.Physical origin of the forward mass movement

The pores are not self-propelled. For a 30 µm pore in liquid 316L the viscous response time is 29 µs, so the Stokes number is 0.12 at 4 kHz and 0.03 at 1 kHz. A pore relaxes to the local melt velocity within a small fraction of one cycle and therefore reports the flow rather than its own dynamics [24]. The recordings carry an internal check on the velocity scale, since pores captured by the solidification front drift rearward at 5.9 µm/ms against the 6.0 µm/ms imposed by the stage, which confirms the scale and the sign convention with nothing fitted. Buoyancy cannot account for the motion. Rise for the same pore is 0.86 µm/ms, under two percent of the measured speed, and it acts vertically rather than along the weld [23,25]. The transport is directed, it appears only above a threshold amplitude, and its magnitude depends on how the dwell time is split between the two points. These are properties of the surrounding melt, not of a force acting on an isolated pore.

The melt is driven by the pressure difference between the two keyholes. The rear keyhole forms in preheated material and is the deeper and wider of the two, so its wall runs hotter and its recoil pressure is higher. Sustaining the measured flow over the 800 µm between the dwell points, through a layer about 110 µm thick, requires 229 Pa. Recoil pressure at the boiling point of iron is 55 kPa and changes by 228 Pa per kelvin [26], so this corresponds to about one kelvin between the two keyhole walls. The mechanism costs almost nothing to sustain, which is why the forward bias appears wherever the two dwell points are thermally distinct. Amplitude decides whether that pressure dipole exists. The oscillation Fourier number, the ratio of the thermal diffusion length to the dwell separation, is 0.48 at 48 µm, 0.03 at 200 µm and below 0.01 at 800 µm. At small amplitudes the two heating points lie inside one another's thermal field and merge into a single source, so there is no asymmetry and no directed flow. Without oscillation the pores split evenly between forward and rearward, which is no net transport. The forward fraction departs from one half only once the amplitude exceeds the keyhole width, reaching 0.82 at 400 µm and 0.88 at 800 µm.

Frequency controls how continuous the transport is rather than whether it occurs. Mean forward speed rises from 15.6 µm/ms at 1 kHz to 49.8 µm/ms at 4 kHz. At 1 kHz the interval between visits lets the front keyhole decay and the intervening melt become sluggish, and each dwell point acts largely on its own. Higher frequency shortens that interval below the decay time of the keyhole, the two points stay coupled and the flow between them persists through the cycle. The gain is partly offset by the finite response of the scanner and the melt, since the effective amplitude is 79 % of the commanded 800 µm at 4 kHz against the full value at 1 to 3 kHz. The dwell distribution sets how hard the pair is driven. Forward transport needs the rear point as a pressure source and the front point as a sink, and biasing the cycle toward either end weakens one of the two. The balanced pattern keeps both and gives 49.8 µm/ms, the front heavy pattern 38.6 µm/ms, and the back heavy pattern 18.1 µm/ms, because a long rear dwell starves the front keyhole and removes the sink toward which the melt is drawn. The melt Péclet numbers are 8.9, 6.9 and 3.2, so forward advection dominates thermal diffusion in all three but by a margin that differs almost threefold.

The result is a transfer of mass. The balanced pattern gives a forward flux of 2.5 nL per second, or 17.6 mg of melt per second, which is half a percent of the pool volume per cycle. Material spends about 133 ms in the pool at 6 mm/s, so its contents are swept from rear to front some 2.7 times before solidification. This is the quantity that connects the oscillation to multi material joining, where the useful output is not the shape of the fusion zone but the number of times its contents are turned over [27].

4. CONCLUSIONS

This work investigated a custom longitudinal two-point wobbling strategy for laser welding of 316L steel, combining metallographic cross sections with in situ X ray experiments to link melt pool

geometry to keyhole dynamics and to the flow within the pool. Three pattern variants (balanced, front heavy, and back heavy) were examined, with amplitude (A) and frequency (f) varied independently. The melt pool geometry is directly controlled by A, which is the distance between the two dwell points. Below approximately 50 µm the effect is negligible, however as A increases the melt pool becomes wider and shallower. Beyond A ≈ 400 µm it adopts an onion like shape for pattern 1, whereas this transition occurs only at about 500 to 600 µm for patterns 2 and 3. Pattern 1 maintains the greatest penetration depth up to A ≈ 450 µm, although its surface width decreases sharply at A = 400 µm. These trends indicate a transition in keyhole behavior: deep and stationary at low amplitudes, following the oscillation from A ≈ 200 µm, and forming only at the dwell extremities at the largest amplitudes. The rear keyhole is consistently larger than the front one, suggesting higher temperatures where the beam re-enters already heated material.
This thermal asymmetry sets up a recoil pressure difference between rear and front that drives melt forward along the pool, carrying pores from the back to the front where they are reabsorbed at the front keyhole. Automated tracking of every pore across the recordings quantifies this transport. Without oscillation the pores divide evenly between forward and rearward motion, which is no net transport, whereas the forward fraction reaches 0.82 at A = 400 µm and 0.88 at A = 800 µm. At A = 800 µm and f = 4 kHz the mean forward velocity relative to the surrounding material is 49.8 µm/ms for the balanced pattern, 38.6 µm/ms for the front heavy pattern and 18.1 µm/ms for the back heavy pattern, corresponding to a forward mass flux of 17.6 mg/s and to the pool contents being swept from rear to front about 2.7 times before solidification. A Stokes number below 0.12 and a buoyant rise speed of 0.86 µm/ms, under two percent of the measured velocity, establish that the pores follow the melt rather than moving under their own buoyancy, and the required pressure difference of 229 Pa is only four parts in a thousand of the recoil pressure, so the mechanism is easily sustained. The porosity area in the synchrotron videos is greatest at A = 200 µm and lowest at A = 800 µm. Frequency controls how fully the keyholes develop and how continuous the transport is: at 4 kHz the measured dwell separation is 628 µm, 79 % of the imposed 800 µm, because the keyholes begin forming ahead of the dwell points and cannot fully develop before the beam reverses, whereas at 1 to 3 kHz the full amplitude is recovered. Overall, the longitudinal two-point wobble provides a controllable approach to tailoring melt pool shape, keyhole dynamics and internal mass transport, with dwell distribution, amplitude and frequency acting as coupled parameters governing penetration, width, residual porosity and the rate at which the pool contents are carried forward.

5. DECLARATIONS

CRediT authorship contribution statement

E.S. conceptualized the study. A.W. carried out the experimental work and prepared the original draft of the manuscript, with E.S., P.Y. and A.R. contributed to the experimental work. A.W. performed the material characterization, and A.W. and C.R. carried out the data analysis. C.R. contributed to the software design and analysis. P.H. and E.I. provided resources. All authors contributed to the interpretation of the results, revised the manuscript, and approved the final version.

Declaration of Competing Interest

The authors declare that they have no known competing financial interests or personal relationships that could have appeared to influence the work reported in this paper.

Data availability

The in situ synchrotron radiography recordings analyzed in this study are provided as supplementary videos. The derived pore trajectory data and the analysis scripts are available from the corresponding author on reasonable request.

Acknowledgements
The authors acknowledge the European Synchrotron Radiation Facility for provision of beamtime at beamline ID19, and thank the beamline staff for assistance.

Funding declaration
The authors received no financial support for the research, authorship, or publication of this article.

6. REFERENCES

[1] S. Sanati, S.F. Nabavi, R. Esmaili, A. Farshidianfar, H. Dalir, A Comprehensive Review of Laser Wobble Welding Processes in Metal Materials: Processing Parameters and Practical Applications, Lasers Manuf. Mater. Process. 11 (2024) 492–528. https://doi.org/10.1007/s40516-024-00245-w.

[2] I.J. Spalding, Laser systems development, Phys. Bull. 22 (1971) 401. https://doi.org/10.1088/0031-9112/22/7/013.

[3] A. Klimpel, Review and Analysis of Modern Laser Beam Welding Processes, Materials 17 (2024) 4657. https://doi.org/10.3390/ma17184657.

[4] Z. Li, C. Ren, J. Lv, Y. Geng, B. Li, L. Wang, B. Lu, Eliminating pores and achieving isotropic properties in Al-Cu alloy by high-power oscillating laser-arc hybrid additive manufacturing, Additive Manufacturing 121 (2026) 105146. https://doi.org/10.1016/j.addma.2026.105146.

[5] W. Huang, W. Cai, T.J. Rinker, J. Bracey, W. Tan, Effects of laser oscillation on metal mixing, microstructure, and mechanical property of Aluminum–Copper welds, International Journal of Machine Tools and Manufacture 188 (2023) 104020. https://doi.org/10.1016/j.ijmachtools.2023.104020.

[6] K. Hao, G. Li, M. Gao, X. Zeng, Weld formation mechanism of fiber laser oscillating welding of austenitic stainless steel, Journal of Materials Processing Technology 225 (2015) 77–83. https://doi.org/10.1016/j.jmatprotec.2015.05.021.

[7] M. Kraetzsch, J. Standfuss, A. Klotzbach, J. Kaspar, B. Brenner, E. Beyer, Laser Beam Welding with High-Frequency Beam Oscillation: Welding of Dissimilar Materials with Brilliant Fiber Lasers, Physics Procedia 12 (2011) 142–149. https://doi.org/10.1016/j.phpro.2011.03.018.

[8] S.M.H. Hojjatzadeh, N.D. Parab, W. Yan, Q. Guo, L. Xiong, C. Zhao, M. Qu, L.I. Escano, X. Xiao, K. Fezzaa, W. Everhart, T. Sun, L. Chen, Pore elimination mechanisms during 3D printing of metals, Nat Commun 10 (2019) 3088. https://doi.org/10.1038/s41467-019-10973-9.

[9] F. Galbusera, L. Caprio, B. Previtali, A.G. Demir, The influence of novel beam shapes on melt pool shape and mechanical properties of LPBF produced Al-alloy, Journal of Manufacturing Processes 85 (2023) 1024–1036. https://doi.org/10.1016/j.jmapro.2022.12.007.

[10] L. Wang, M. Gao, C. Zhang, X. Zeng, Effect of beam oscillating pattern on weld characterization of laser welding of AA6061-T6 aluminum alloy, Materials & Design 108 (2016) 707–717. https://doi.org/10.1016/j.matdes.2016.07.053.

[11] T. Girerd, A. Gameros, M. Simonelli, A. Norton, A.T. Clare, Modulation of melt pool behaviour using novel laser beam oscillation methods, Journal of Materials Processing Technology 325 (2024) 118300. https://doi.org/10.1016/j.jmatprotec.2024.118300.

[12] J. Cai, Z. Ouyang, H. Jin, Y. Kong, Y. Wei, Study on oscillating laser welding of 6061-T6 aluminum alloy medium-thick plate: Energy distribution, joint forming, texture evolution, and mechanical properties, Optics & Laser Technology 188 (2025) 112910. https://doi.org/10.1016/j.optlastec.2025.112910.

[13] J. Svenungsson, I. Choquet, A.F.H. Kaplan, Laser Welding Process – A Review of Keyhole Welding Modelling, Physics Procedia 78 (2015) 182–191. https://doi.org/10.1016/j.phpro.2015.11.042.

[14] W. Suder, X. Chen, D.R. Sierra, G. Chen, J. Wainwright, K. Rajamudili, G.R. Pardal, S. Williams, Control of meltpool shape in laser welding, Weld World 68 (2024) 1485–1495. https://doi.org/10.1007/s40194-024-01719-3.

[15] M.J. Matthews, T.T. Roehling, S.A. Khairallah, T.U. Tumkur, G. Guss, R. Shi, J.D. Roehling, W.L. Smith, B.K. Vrancken, R.K. Ganeriwala, J.T. McKeown, Controlling melt pool shape, microstructure and residual stress in additively manufactured metals using modified laser beam profiles, Procedia CIRP 94 (2020) 200–204. https://doi.org/10.1016/j.procir.2020.09.038.

[16] S. Sanati, S.F. Nabavi, A. Farshidianfar, Laser wobble welding modeling process: A comprehensive review of fundamentals, methods, heating, and solidification modes, Journal of Manufacturing Processes 131 (2024) 1703–1739. https://doi.org/10.1016/j.jmapro.2024.10.001.

[17] K. Matsuda, N. Ramachandiran, A.P. Gerlich, Improved fillet weld quality in AA 7075 sheets using flower pattern laser wobbling, Optics & Laser Technology 192 (2025) 113438. https://doi.org/10.1016/j.optlastec.2025.113438.

[18] A. Das, T. Dale, I. Masters, D. Widanage, Feasibility of Fillet Edge Weld Using Laser Wobble Technique, Procedia CIRP 95 (2020) 846–851. https://doi.org/10.1016/j.procir.2020.03.129.

[19] M.C. Asirvatham, I. Masters, G. West, P. Haney, High-brightness laser welding with beam wobbling: Achieving high-strength Al/Steel joints for battery busbars, Journal of Advanced Joining Processes 11 (2025)

100305. https://doi.org/10.1016/j.jajp.2025.100305.
[20] Y. Ai, J. Liu, C. Ye, J. Cheng, Influence of oscillation parameters on energy distributions and dynamic behaviors during laser welding of aluminum alloy T-joints assisted with solder patch, International Journal of Thermal Sciences 201 (2024) 108953. https://doi.org/10.1016/j.ijthermalsci.2024.108953.
[21] A. Rack, F. Garcia-Moreno, C. Schmitt, O. Betz, A. Cecilia, A. Ershov, T. Rack, J. Banhart, S. Zabler, On the possibilities of hard X-ray imaging with high spatio-temporal resolution using polychromatic synchrotron radiation, Journal of X-Ray Science and Technology 18 (2010) 429–441. https://doi.org/10.3233/XST-2010-0273.
[22] W. Li, R. Lambert-Garcia, A.C.M. Getley, K. Kim, S. Bhagavath, M. Majkut, A. Rack, P.D. Lee, C.L.A. Leung, AM-SegNet for additive manufacturing in situ X-ray image segmentation and feature quantification, Virtual and Physical Prototyping 19 (2024) e2325572. https://doi.org/10.1080/17452759.2024.2325572.
[23] K.C. Mills, Recommended Values of Thermophysical Properties for Selected Commercial Alloys, Woodhead Publishing, Cambridge, 2002.
[24] M.R. Maxey, J.J. Riley, Equation of motion for a small rigid sphere in a nonuniform flow, Phys. Fluids 26 (1983) 883–889. https://doi.org/10.1063/1.864230.
[25] R. Clift, J.R. Grace, M.E. Weber, Bubbles, Drops, and Particles, Academic Press, New York, 1978.
[26] V. Semak, A. Matsunawa, The role of recoil pressure in energy balance during laser materials processing, J. Phys. D: Appl. Phys. 30 (1997) 2541–2552. https://doi.org/10.1088/0022-3727/30/18/008.
[27] T. DebRoy, S.A. David, Physical processes in fusion welding, Rev. Mod. Phys. 67 (1995) 85–112. https://doi.org/10.1103/RevModPhys.67.85.

Supplementary Files

This is a list of supplementary files associated with this preprint. Click to download.

- supplementalmaterial.pdf